High-efficiency sub-microscale uncertainty measurement method using pattern recognition

ABSTRACT: This study presents a fast precision measurement method that uses pattern recognition. First, a specific micro-structured surface with nanometre precision was designed and manufactured. The micro-structure was composed of equi-spaced concentric circles and straight lines with a spacing of 50 μm, providing a unique pattern for recognition and matching. Second, a measurement system was proposed based on four algorithms. A circle Hough transform (CHT) based algorithm was adopted to recognise the pattern quickly and significantly reduce the search area. A trained neural network was used to improve the recognition accuracy, and the template matching (TM) and sub-pixel interpolation (SI) algorithms were used for precise positioning with nanoscale resolution. Then, a series of experiments were carried out to prove the validity of the developed methodology from three aspects: circle detection, length uncertainty, and measurement speed and range. The experimental results showed that the percentage of the correct circle classification was more than 96% and the CHT search accuracy was within a two-pixel level. This means that the number of pixels that matched reduced from a million to a single digit; hence, the calculation time was greatly reduced. A length uncertainty test demonstrated that the proposed measurement method was able to achieve 90-nm length uncertainty, and a comparison of measurement speeds showed that it helped to speed up measurements by a factor of 1000 compared to the original method.

Keywords: Precision measurement; Neural network; Image processing; Polar microstructure

1 Introduction

Measurements are typically taken to obtain the displacement or the distance of an objective point relative to a reference point. Generally, precision positioning measurement can be described as a technology or method that can provide a resolution better than 0.1 μm or a relative positioning error of less than 10^{-6} [1]. Optical sensors are widely applied in precision measurements because of their non-contact nature, wide bandwidth, and high resolution. A variety of optical sensors are available that are

based on different principles, such as the time-of-flight distance, laser interferometer, and optical encoders. As air refractive index and wavelength errors are their main sources of uncertainty, a stringent environment (including atmospheric pressure, temperature, humidity, and medium) is needed to control these sources of uncertainty. Moreover, the number of components involved in currently available sensors is so large that they require a large space for installation and high assembly accuracy, thus opening up the possibility for more systemic errors and costs.

With the rapid development of image processing technologies, numerous vision-based precision measurement methods have emerged [2–4]. Vision-based measurement technology is based on machine vision and the integration of optoelectronics and image processing technologies, to form a comprehensive measurement system [5, 6]. Equipment based on vision-based measurement technology can realise intelligent, digital, network and other multi-functions, as well as miniaturisation. Compared to the other popular alternatives, vision-based measurements have high efficiency, high precision, simple structure, low cost, and non-destructive detection features; hence, they can meet the requirements of modern measurement technologies. This has been applied in precision positioning over recent decades [7–9]. Compared to the traditional surface encoder, this method obtains the absolute position with vision-based principles instead of laser scanning. However, it mostly measures in a linear direction and has the shortcoming of inadequate resolution. A number of vision-based measurement research studies have been conducted in recent times and can be found in the literature [10–13]. For example, Clark et al. [14] proposed a vision-based measurement methodology that utilises a micrometre calibration slide and a confocal microscope. This technique overcomes the shortcomings of limited charge coupled device (CCD) pixel count and image size, out of focus areas at the boundaries of the image, and vertical motion of the slide out of the focal plane. A novel 2D intertwined pattern was also proposed for two-axis precision measurement [15–17]. This method uses a pseudo-periodic pattern observed with a microscope head and a CCD camera. This micrometric pattern corresponds to the intertwining of two perpendicular copies of a single-axis pattern made of two frequency carriers with slightly different periods. In addition, another novel vision-based planar encoder was proposed for absolute high-precision three degrees-of-freedom position measurement [18]. This planar encoder is composed of a grating and a black-and-white (B/W) camera that captures the images of the grating. The grating has a periodic grid pattern with embedded codes for absolute position measurement. By decoding the embedded codes, absolute position measurement can be taken with a resolution equal to the pitch of the grid pattern. This research has been

further extended to contribute to the rapid development of vision-based precision measurement [19–23]. It is worth noting that most of the above research methods used periodic patterns as a reference for positioning. However, they require very high manufacturing accuracy of the patterns and their calibration cost cannot be ignored. Recently, a novel precision measurement method based on template matching (TM) theory has been proposed [24–27]. Contrary to the abovementioned methods, this method first uses non-periodic patterns as a reference, which reduces the requirement of component accuracy and eliminates the calibration process; however, its calculation efficiency is quite low.

The current limitations of vision-based measurement techniques mainly relate to two aspects. First, most of the current theories and principles are based on a periodic pattern and the phase shift principle, integrated with a relatively simple algorithm. They have a common shortcoming in that they require a high-accuracy micro-pattern, which in turn entails much higher calibration costs. In other words, the current research can be considered as 'vision-based precision measurement', and not 'computer vision-based measurement'. Second, although the TM-based method using a non-periodic pattern has been investigated and can achieve 150-nm length uncertainty, its low calculation efficiency is still a shortcoming for the application. Many studies have aimed to improve the calculation speed of TM by using techniques such as bounded partial correlation, pyramidal decomposition, and real-time object tracking [28–30]; however, they mostly focussed on the general conditions, and problems related to the uncertainty of matching results and resolution persist.

To address the above-mentioned problems, this study proposes the use of pattern recognition to develop a fast nanoscale measurement method. The aim of the pattern recognition algorithms is to improve the measurement stability, reduce the requirements of measurement hardware, and increase efficiency. The remainder of the paper is organised as follows. Section 2 presents the designed microstructure surface for the positioning reference (global search map). Section 3 explains the architecture of the measurement system and introduces the related algorithms. In Section 4, a series of experiments that were carried out to validate the performance of the proposed method are detailed. Finally, some conclusions are given in Section 5.

2 Generation of polar microstructure

There are only a few related studies on improving the resolution and precision of computer vision, because most of the applied fields of computer vision are at a macroscopic scale. However, resolution

and precision are key requirements in precision measurements. To improve the resolution, microscopic observation of the target is an important solution; however, it is difficult to obtain a high distinction rate on most natural object surfaces using microscopic observation. In this case, specially designed micro-structured surfaces are necessary to improve the surface resolution. Moreover, considering the measurement performance mainly relies on the ability of pattern recognition, the requirement of the surface texture should be stringent. The manufacturing difficulty and efficiency should also be considered. In summary, the designed surface structure should meet all the following requirements: (1) high resolution of pattern recognition at the microscopic scale; (2) unique pattern distributed in the global map of the structure surface; (3) easy to recognise circles; (4) sub-microscale machining accuracy; and (5) simple manufacturing process and high productivity.

Ultra-precision machining (UPM) can achieve a surface roughness of a few nanometres and an accuracy of sub-micrometres [31]. Hence, a surface texture named ‘polar microstructure’ was manufactured by utilising UPM, as shown in Fig. 1. The surface features of the polar micro-structured surface consist of concentric circles and straight lines with equal spacing of 50 μm. The surface was fabricated by a process chain of UPM technology, which combined single point diamond turning (SPDT) and single point diamond broaching (SPDB). The circles are designed for subsequent circle detection, and the combination of straight lines and circles forms a unique pattern, which is significantly different from the other methods with periodic patterns. Therefore, the intensity distribution of the images of the polar microstructure is not only unique; it also remains unique when there are machining errors on the polar microstructure surface. This avoids low-efficiency calibration. Moreover, each intersection of a line and a circle forms a feature point, as shown in Fig. 1. This is important for subsequent recognition, owing to the sudden change in pixel gradient around the feature point. If the circles of the polar

microstructure can be detected, the position of the circle centre can be found; hence, the current absolute position can be estimated.

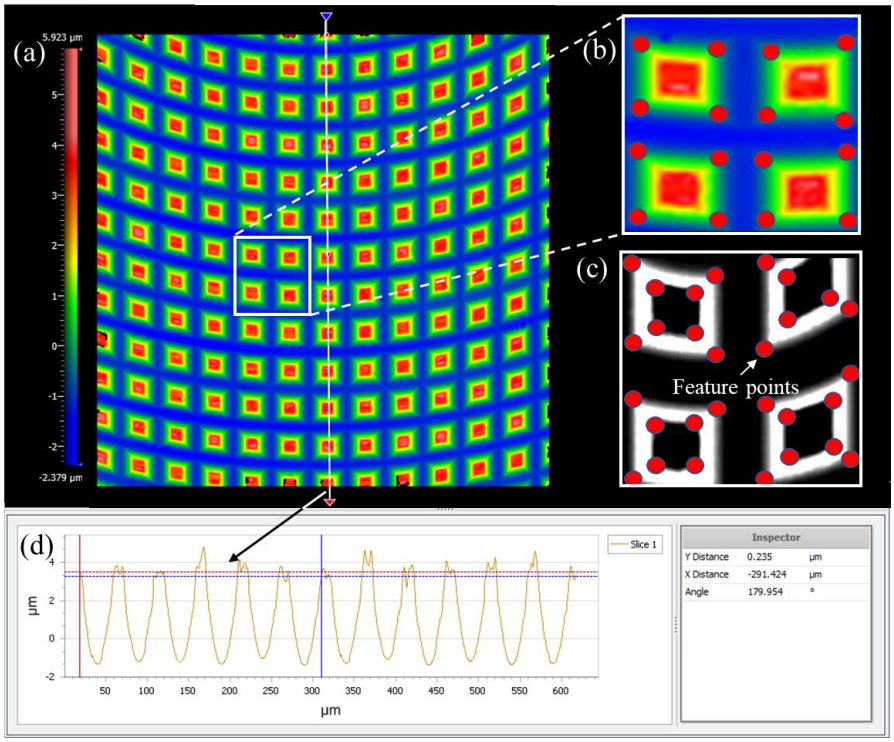

Fig. 1 Surface texture of the polar microstructure: (a) observed with a Zygo optical surface profiler, (b) manufactured feature points, (c) detected feature points and (d) groove spacing.

3 Measurement system

3.1 Overview of the system architecture

Circle detection is an interesting topic in pattern recognition. A change in illumination (or other environmental noises) will cause difficulties in detecting the circle features, and the accuracy of positioning the circle centre will be difficult to guarantee. At the same time, another crucial problem is the computational efficiency, which decides the measurement time. Hence, the pattern recognition should be accurate, robust, and fast in the measurement system. Taking these issues into consideration, Fig. 2 shows the measurement process of the proposed system. The polar microstructure and a CCD camera are

prepared beforehand, and the actual position (x_0, y_0) is recorded using the image captured by the CCD camera. In the first stage, the circle Hough transform (CHT) algorithm aims to find the coordinates (x_1, y_1) of the circle centre in the current image, followed by the absolute position (x_2, y_2) of the current image in the global map. A neural classifier (NC) algorithm is used to guarantee that the circle detection by CHT is correct, and if it is not, the detection will be conducted again. Next, a TM algorithm is applied to match only within a few pixels of the surrounding area of (x_2, y_2), with the matching result being the precise position (x_3, y_3). A sub-pixel interpolation (SI) algorithm is used to improve the resolution and then re-match to obtain a more precise position (x_4, y_4), which is the final measurement result. The measurement uncertainty is the error between (x_4, y_4) and (x_0, y_0). The architecture of the proposed measurement system is summarised in Fig. 3.

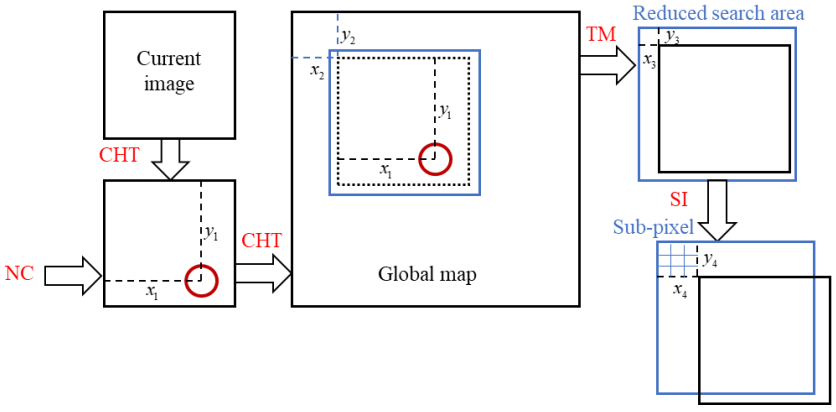

Fig. 2 Processes of the measurement system.

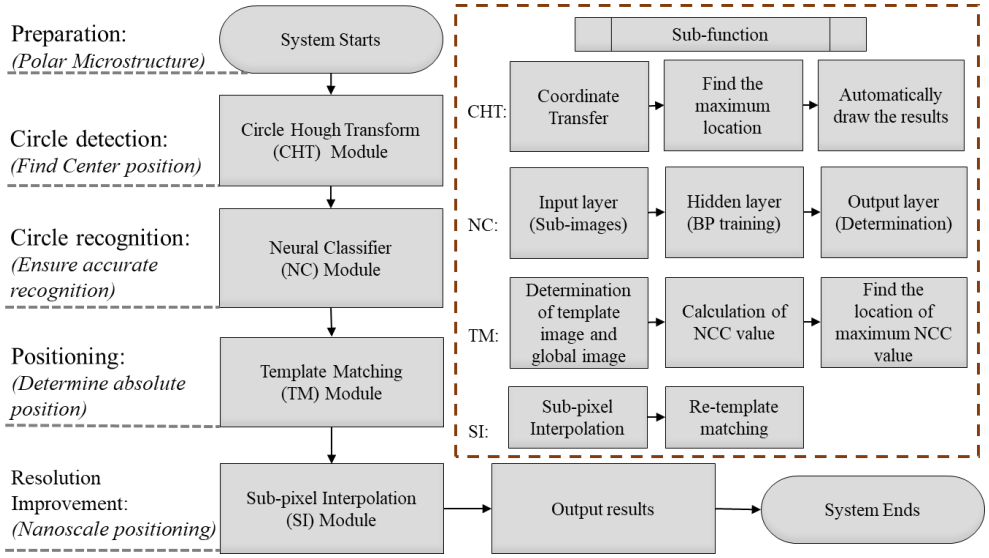

Fig. 3 Architecture of the measurement system.

3.2 Circle detection with circle Hough transform

The Hough transform [32] is a feature extraction technique used in image analysis and processing. As a specialisation of Hough transform, CHT [33] is a process of converting a circle in an 'image space' into a point in the parameter space called 'output accumulator space'. A circle with radius R centred at (α, β) can be described as follows:

$$(x-\alpha)^2+(y-\beta)^2=R^2 \tag{1}$$

There are three degrees-of-freedom coordinates: α, β, and R. The general equation for a circle can be expressed in a different way by performing a coordinate transformation from x–y coordinate system to α–β coordinate system and can be written in the following form:

$$(\alpha-x)^2+(\beta-y)^2=R^2 \tag{2}$$

Then, a point on the circular boundary in the x–y coordinate system corresponds to a circle in the α–β coordinate system as shown in Fig. 4. As the points in the original image are all on the same circle,

the transformed α and β must also satisfy all the circular equations in the α–β coordinate system. The circles corresponding to all such points will intersect at one point, and the intersection point is the centre (α, β). Subsequently, the number of circles at the local intersection is counted. Each local maximum is considered to obtain the corresponding circle centre coordinates (α, β) in the original image. Once a circle is detected under a certain R, the coordinate of the circle can also be determined.

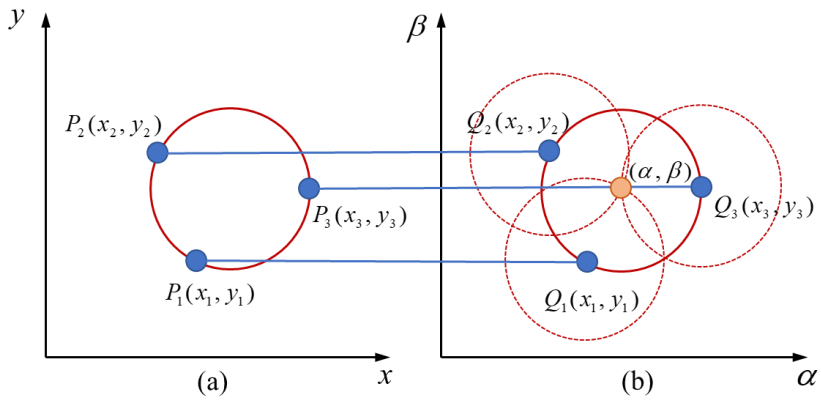

Fig. 4 Illustration of the CHT algorithm: (a) Image space, and (b) output accumulator space.

Expressing the above mathematically, the circle detection operator is defined as that which is suitable for all the image pixels to produce a maximum, when a circle with its radius within the range of $[R_{\min}, R_{\max}]$ is detected:

$$u(x,y) = \frac{\iint_{D(x,y)} \vec{e}(\alpha,\beta)\cdot\vec{O}(\alpha-x,\beta-y)\mathrm{d}\alpha\mathrm{d}\beta}{2\pi(R_{\max}-R_{\min})} \tag{3}$$

where domain $D_{(x,y)}$ is defined as follows:

$$D_{(x,y)} = \left\{(\alpha,\beta)\in\Re^2 \mid R_{\min}^2 \le (\alpha-x)^2+(\beta-y)^2 \le R_{\max}^2\right\} \tag{4}$$

$\vec{e}$ is the gradient vector:

$$\vec{e}(x,y)=\left[\frac{E_x(x,y)}{|E|},\frac{E_y(x,y)}{|E|}\right]^{\mathrm{T}} \tag{5}$$

and $\vec{O}$ is the kernel vector:

$$\vec{O}(x,y)=\left[\frac{\cos(\tan^{-1}(y/x))}{\sqrt{x^2+y^2}},\frac{\sin(\tan^{-1}(y/x))}{\sqrt{x^2+y^2}}\right]^{\mathrm{T}} \tag{6}$$

When the entire circle is not displayed in the image, the $\vec{O}(x,y)$ operator is modified to detect semicircles and is re-defined as follows:

$$\vec{O}(x,y)=\begin{cases}\left[\dfrac{\cos(\tan^{-1}(\frac{y}{x}))}{\sqrt{x^2+y^2}},\dfrac{\sin(\tan^{-1}(\frac{y}{x}))}{\sqrt{x^2+y^2}}\right]^{\mathrm{T}} & y\geq x(\tan(\vartheta)) \\ [\cos(\vartheta\text{-}90^\circ),\sin(\vartheta\text{-}90^\circ)]^{\mathrm{T}} & |y-x(\tan(\vartheta))|\leq\dfrac{R_{\max}-R_{\min}}{2} \\ 0 & \text{otherwise}\end{cases} \tag{7}$$

where ϑ is the slope of the semicircle diameter.

To characterise the frequencies of the image and localise them quickly, a 2D wavelet transform is used to convert the input image into wavelet coefficients at a lower resolution level. The main feature of the wavelet transform is that it can fully highlight some aspects of the problem through transformation, locally analyse the space frequency, gradually multi-scale the signal function through the telescopic translation operation, and finally reach a high frequency. Time subdivision and frequency subdivision at low frequency can automatically adapt to the requirements of the time-frequency signal analysis, so that it can focus on any detail of the signal and solve the difficult problem of Fourier transform. The wavelet transform operator $F:L^2(R)\rightarrow L^2(R)$ can be defined as:

$$F(f(s)) = \hat{f}(s) = \int_{-\infty}^{\infty} f(u)\psi_{s,t}(u)\mathrm{d}u \tag{8}$$

where the mother wavelet function is described as:

$$\psi_{s,t}(u) = \frac{1}{|s|^p}\psi(\frac{u-t}{s}), \quad \psi(t) = \begin{cases} 1 & 0 \le t < 1/2 \\ -1 & 1/2 \le t < 1/2 \\ 0 & \text{otherwise} \end{cases} \tag{9}$$

By varying s, the frequencies on which the function ψ operates are changed; p is the power of the absolute value of s and by varying t, the function ψ is moved on all supports of the function f.

For the polar microstructure, let the concentric circle with the smallest radius (C_0) be used as the identifier. The detected centre of C_0 in the image is used to determine the current position range. Then a follow-up match is conducted only in the estimated range, which is much smaller than the global searching range of the previous TM. The reason for choosing C_0 as the identifier is that C_0 is located at the centre of the surface and appears on the images in most measurement situations. Moreover, the radius of curvature of C_0 is the smallest, which is the easiest and the most accurate to be recognised by the CHT algorithm.

3.3 Circle recognition with a neural classifier

While the CHT algorithm finds the location of the image containing the circle, the NC algorithm aims to determine if the identified circle is accurate. Because the detection error causes the actual position to be not in the search range, it seriously affects the measurement accuracy and a further circle recognition process is necessary for the measurement system. Here, a multi-layer feedforward neural network trained with a back propagation (BP) algorithm is applied for the circle recognition. The neural network consists of three layers of nodes, as shown in Fig. 5. The number of nodes in the input layer depends on the number of coefficients selected after image preprocessing. The hidden layer has many nodes, and the

output layer has only two nodes to justify whether it is a circle. The rationale behind the BP algorithm has been described in detail in [34]. In general, the core idea of the BP algorithm is to compare the output results with the real results through a continuous iteration, constantly change the weight values between the nodes according to the results, and improve the accuracy through continuous training. Here, a process using a BP-based neural network to classify the circle is introduced. Fig. 6 (a) shows the input image of the polar microstructure used for pattern recognition, with 1mm-square area. Fig. 6(b) shows a sub-image of the polar microstructure containing the circle, and it is chosen as one of the samples to train the BP algorithm.

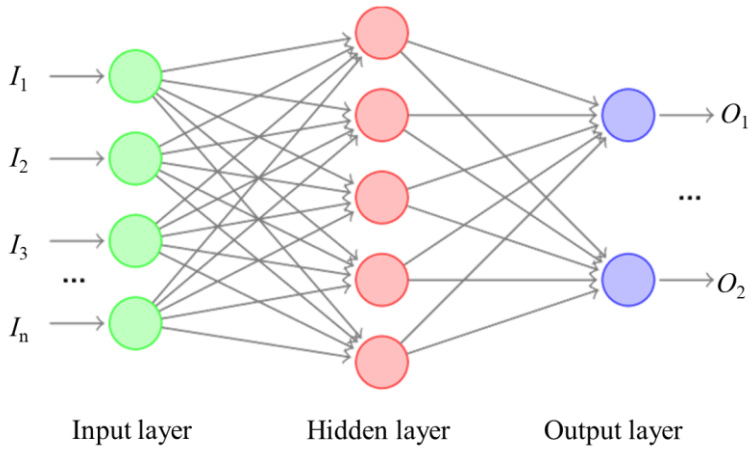

Fig. 5 A multi-layer feedforward neural network.

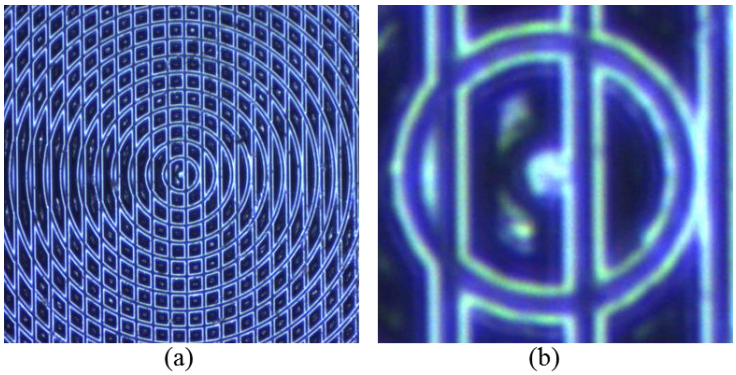

Fig. 6 (a) The input image of the polar microstructure used for pattern recognition (b)Sample sub-image of the

polar microstructure detected by the CHT algorithm.

As for the input layer, while training the neural network, the difference between different input layers should be large enough to be easily distinguished at an early stage. For the image processing, the ratio of grey values is within the range of 0–255. Hence, ratio of grey values greater than 200 I_1, and a ratio less than 30 I_2 (shown in Fig. 5) are chosen as the two coefficients to describe the pattern depicted in Fig. 6. As shown in Fig. 7, I_1, I_2 and the offset b_1 consist of the nodes in the input layers. The second layer is the hidden layer. For the convenience of description, it only contains two nodes H_1 and H_2 and the offset b_2. The third layer comprises the outputs O_1 and O_2, where O_1 represents the probability that the input image is not a circle and O_2 represents the probability that the input image is a circle. w_i of each line is the weight of the connection between the layers. The activation function defaults to the sigmoid function because its derivatives facilitate subsequent calculations. Before the algorithm starts, initial values are assigned to each parameter as shown in Table 1. As Fig. 6 contains a circle, which means that the probability of containing a circle is close to 1 ($O_2 = 1$) and the probability of not containing a circle is close to zero ($O_1 = 0$), the goal of the BP algorithm is to give input data I_1 and I_2, such that the output is as close as possible to the target outputs O_1 and O_2.

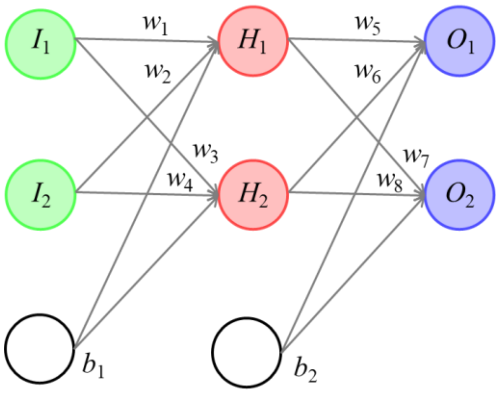

Fig. 7 Simplified neural network for pattern recognition training.

Table 1 Initial values of each parameter in the neural network algorithm

Parameters	Symbol	Initial value
Input layer	I_1	0.05
	I_2	0.10
Output layer	O_1	0.01
	O_2	0.99
Offset	b_1	0.30
	b_2	0.60
Weight coefficient	w_1	0.15
	w_2	0.20
	w_3	0.25
	w_4	0.30
	w_5	0.40
	w_6	0.45
	w_7	0.50
	w_8	0.55

The algorithm contains two main links: forward propagation and back propagation. For the forward propagation, the process is conducted from the input layer to the hidden layer and then to the output layer. For the back propagation the reverse is true. For the process of input layer to hidden layer, the input weighted sum of nodes H_1 can be calculated by [35] as follows:

$$net_{H1} = w_1 \cdot I_1 + w_2 \cdot I_2 + b_1 = 0.3775 \tag{10}$$

The output O_1 of node H_1 is calculated (the activation function used here is the sigmoid function) as:

$$out_{H1} = \frac{1}{1+e^{-net_{H1}}} = 0.5933 \tag{11}$$

Similarly, the output O_2 of node H_2 can be calculated as:

$$out_{H2} = 0.5969 \tag{12}$$

For the process of hidden layer to output layer:

$$net_{O1} = w_5 \cdot out_{H1} + w_6 \cdot out_{H2} + b_2 = 1.1059 \tag{13}$$

$$out_{O1} = \frac{1}{1+e^{-net_{O1}}} = 0.7514 \tag{14}$$

Using a similar method, it has $out_{O2} = 0.7729$. With this, the process of forward propagation is over and the output value [0.7514, 0.7729] is obtained, which is far from the actual value [0, 1]. This error should be reduced by updating the weight and recalculating the output, which is actually the back-propagation process. As there are two outputs, the errors of O_1 and O_2 (E_{01} and E_{02}, respectively) can be calculated separately as follows:

$$E_{O1} = \frac{1}{2}(target_{O1} - out_{O1})^2 = 0.5 \times (0.01 - 0.7514)^2 = 0.2748, \quad E_{O2} = 0.0236 \tag{15}$$

The total error is the sum of the two errors:

$$E_t = E_{O1} + E_{O2} = 0.2984 \tag{16}$$

Subsequently, the weight is updated from the hidden layer to the output layer. Taking the weight parameter w_5 as an example, to know how much influence w_5 has on the overall error, the overall error is used to find the partial derivative of w_5 according to the chain rule:

$$\frac{\partial E_t}{\partial w_5} = \frac{\partial E_t}{\partial out_{O1}} \cdot \frac{\partial out_{O1}}{\partial net_{O1}} \cdot \frac{\partial net_{O1}}{\partial w_5} \tag{17}$$

The value of each term in the formula is calculated separately as follows:

$$\frac{\partial E_t}{\partial out_{O1}} = -(target_{O1} - out_{O1}) = -0.01 + 0.7514 = 0.7414 \tag{18}$$

$$\frac{\partial out_{O1}}{\partial net_{O1}} = out_{O1}(1 - out_{O1}) = 0.7514 \times (1 - 0.7514) = 0.1868 \tag{19}$$

$$\frac{\partial net_{O1}}{\partial w_5} = out_{H1} = 0.5933 \tag{20}$$

Thus, partial derivative of the overall error E_t with respect to w_5 is calculated by

$$\frac{\partial E_t}{\partial w_5} = \frac{\partial E_t}{\partial out_{O1}} \cdot \frac{\partial out_{O1}}{\partial net_{O1}} \cdot \frac{\partial net_{O1}}{\partial w_5} = 0.8217 \tag{21}$$

Finally, the value of w_5 is updated as

$$w_5^+ = w_5 - \eta \cdot \frac{\partial E_t}{\partial w_5} = 0.4 - 0.5 \times 0.0817 = 0.3589 \tag{22}$$

where η is the learning rate. Similarly, w_6^+, w_7^+ and w_8^+ are updated with $w_6^+ = 0.4087$, $w_7^+ = 0.5113$ and $w_8^+ = 0.5614$, respectively.

To update the weights between the input and the hidden layers (w_1, w_2, w_3, w_4), the method is similar to the above, which can be expressed as:

$$\frac{\partial E_t}{\partial w_1} = \frac{\partial E_t}{\partial out_{H1}} \cdot \frac{\partial out_{H1}}{\partial net_{H1}} \cdot \frac{\partial net_{H1}}{\partial H_1} = \left(\frac{\partial E_{O1}}{\partial out_{H1}} + \frac{\partial E_{O2}}{\partial out_{H1}}\right) \cdot \frac{\partial out_{H1}}{\partial net_{H1}} \cdot \frac{\partial net_{H1}}{\partial H_1} \tag{23}$$

Similarly, the updated weight coefficients are calculated as $w_1^+ = 0.1498$, $w_2^+ = 0.1996$, $w_3^+ = 0.2498$, and $w_4^+ = 0.2995$. With this, the backpropagation method is completed.

Finally, the updated weights are recalculated iteratively. After the first iteration in this example, the total error drops from 0.2984 to 0.2910. After 1000 iterations, the total error is 0.00003 and the output is [0.0069, 0.9941], which proves the effectiveness of the method. The above illustration is a simple example to show the algorithmic process. In the proposed measurement system, the neural network parameters have been found experimentally. Hundreds of images were used in the input layer and the hidden layer consisted of 80 nodes, thus choosing a combination that produces the best results in terms of circle recognition rate.

3.4 Template matching and sub-pixel interpolation

When comparing two images, the question of how to measure the similarities between the two images is a fundamental issue. Therefore, the TM and SI methods are used for precision measurement [25]. The basic principle of TM is to choose the whole surface texture of the polar microstructure as the

global image. A template image is chosen from an arbitrary area of the global image. The matching process starts from the top left corner of the global image and ends at its bottom right corner. The reference image is of the same size as the template image. In the image to be searched, the reference image is moved, and the differences between the reference image and the template image are measured at each position. When the similarity reaches a maximum, the corresponding position is determined. Here, the normalised cross correlation (NCC) has been chosen as the indicator to describe the similarity, which is expressed as follows:

$$NCC_{(u,v)} = \frac{\sum_{i=1}^{m}\sum_{j=1}^{n}[R(u+i,v+j)-\bar{R}(u,v)]\cdot[T(i,j)-\bar{T}]}{\left[\sum_{i=1}^{m}\sum_{j=1}^{n}(R(u+i,v+j)-\bar{R}(u,v))^2\right]^{\frac{1}{2}}\cdot\left[\sum_{i=1}^{m}\sum_{j=1}^{n}(T(i,j)-\bar{T})^2\right]^{\frac{1}{2}}} \tag{24}$$

where $R(u,v)$ represents the reference image of the u^{th} row of the v^{th} column, $\bar{R}(u,v)$ is the greyscale average intensity of the reference image $R(u,v)$, m and n represent the number of pixels of the template image in the horizontal and vertical directions, i and j represent the specific pixel in the template or the reference image and $\bar{T}$ is the greyscale average intensity of the template image T. These values can be defined as follows:

$$\bar{R}(u,v) = \frac{1}{m\cdot n}\sum_{i=1}^{m}\sum_{j=1}^{n}R(u+i,v+j) \tag{25}$$

$$\bar{T} = \frac{1}{m\cdot n}\sum_{i=1}^{m}\sum_{j=1}^{n}T(i,j) \tag{26}$$

The NCC values are delivered in the interval [–1, 1], which means that $NCC = 1$ implies the best possible similarity; whereas, $NCC = -1$ implies that the template and the corresponding image are completely different. As a result, the point (u, v), which presents the best possible resemblance between R and T, and is defined as follows:

$$(u,v) = \arg\max_{(\hat{u},\hat{v})\in A} NCC(\hat{u},\hat{v}) \tag{27}$$

$$A = \{(u,v)\,|\,1 \le \hat{u} \le M-m, 1 \le \hat{v} \le N-n\} \tag{28}$$

where M and N are the pixel size of the global search.

The SI algorithm should be employed after determining u and v to improve the resolution. The pixel and its neighbouring pixels are interpolated with the bilinear interpolation (BI) method. It should be noted that even though the TM and BI methods are time-consuming, the calculation cost will be reduced significantly, when they are combined with the CHT and NC algorithms as described above.

4 Results and discussion

After building up the measurement system, a series of experiments were conducted to validate its performance, which mainly consisted of three parts: (1) the circle of the polar microstructure was detected by the CHT algorithm and recognised by the NC algorithm and the position of the circle was obtained and compared with the actual position; (2) the length uncertainty of the proposed method was analysed; and (3) the measurement speed of the proposed method was compared with the original TM based method.

4.1 Circle detection results

The circle detection experiment was conducted first to investigate the correct classification of circle recognition, which has a significant influence on the stability and speed of the measurement system. For example, the correct classification of ‘circle’ would reduce the subsequent search area and improve the calculation efficiency. Correct classification of ‘no circle’ guarantees the accuracy of measurement and prevents wrong positioning (which causes serious errors). In this experiment, the polar microstructure surface was captured with a microscope camera, as shown in Fig. 8. A total of 858 images of the polar

microstructure were captured, and a different area in each image was chosen to test the stability of the circle detection. The principle of area determination was to select typical examples, and the naming convention for each chosen area was based on the points at both ends of the diagonal of the rectangular area. For example, the whole of the area in Fig. 8 was named A1H8. The types of chosen areas are shown in Table 2, which is divided into two categories: ‘with circle’ and ‘without circle’. There were approximately 50 images in each group, and the images were cropped according to the chosen area type. Subsequently, each image was processed by the CHT and NC algorithms to recognise whether there was a circle with the given radius. The recognition results were compared with the actual conditions to obtain the correct classification in each chosen area, and the results are shown in Table 2.

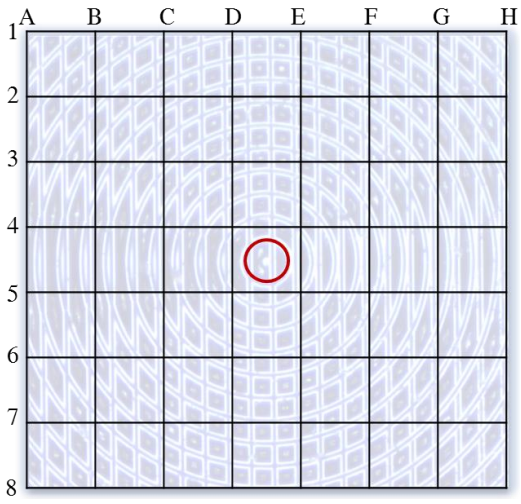

Fig. 8 Captured image of the polar microstructure with the microscope and the division of the chosen area.

It should be noticed that for the group ‘with circle’, the correct classification percentage was over 94.9% and the overall (average) percentage was 96.59%. Thus, the results show that in most conditions, the circle of the polar microstructure, as well as the circle centre position, could be detected correctly to reduce the search area. For the rare situations where the circle could not be detected, only the calculation

cost was incurred, but the measurement accuracy was not influenced. For the group ‘no circle’, the correct classification percentage was higher, i.e., 99.23% and even 100% in some cases. The high classification accuracy guaranteed the accuracy of the search area. For the classification accuracy in different areas of the polar microstructure surface, an analysis was conducted in relation to two aspects. One was from the central area of the polar microstructure with large curvatures of the circular grooves, comprising C2F5, B3E6, C3F6, D3G6 and C4F7. With a total of 254 images and 247 correct detections, its correct classification rate was 97.24%. The other was from the edge area of the polar microstructure with small curvatures of the circular grooves, comprising B2E5, B4E7, D2G5 and D4G7. With a total of 215 images and 206 correct detections, its correct classification rate was 95.81%. Compared to the central area, the edge areas still maintained a reasonably high classification accuracy, even though it was slightly decreased. This difference could be attributed to the number of detected feature points in the edge areas being little less than that of the central area. This reduced the reliability to some extent.

Table 2. The classification performance

Circle				No circle			
Chosen area	Number of images	Number of correct detections	Correct classification (%)	Chosen area	Number of images	Number of correct detections	Correct classification (%)
B2E5	59	56	94.92	A1D4	50	50	100
B3E6	34	34	100	A3D6	63	62	98.41
B4E7	59	57	96.61	A5D8	54	54	100
C2F5	61	60	98.36	C1F4	32	32	100
C3F6	56	54	96.43	C5F8	48	47	97.92
C4F7	40	39	97.5	E1H4	41	41	100
D2G5	48	46	95.83	E3H6	64	63	98.48
D3G6	63	60	95.24	E5H8	37	37	100
D4G7	49	47	95.92				
Overall	469	453	96.59	Overall	389	386	99.23

To determine the accuracy of the CHT algorithm for search positioning exactly, a calibration test was conducted in the global map. The actual area size was 1600 × 1600 μm^2, and the pixel size of the captured image was 2.5 μm in both directions. Therefore, the image contained 640 × 640 pixels. All the 1600 sampling points were evenly distributed on the map with a 40 μm spacing. For each sampling point, the CHT algorithm was used to detect the location of the circle centre and then compare it with its actual location. The pixel error between the above two coordinate values represents the positioning error of the CHT algorithm as shown in Fig. 9. The results show that the average positioning error was 0.63 pixels and the maximum was 1.32 pixels, which indicates that the CHT algorithm helped to reduce the searching area from the global search (usually 1000 × 1000 pixels) to a 4 × 4 pixel search. This greatly reduced the cost of calculation according to Eqs. (24)–(28).

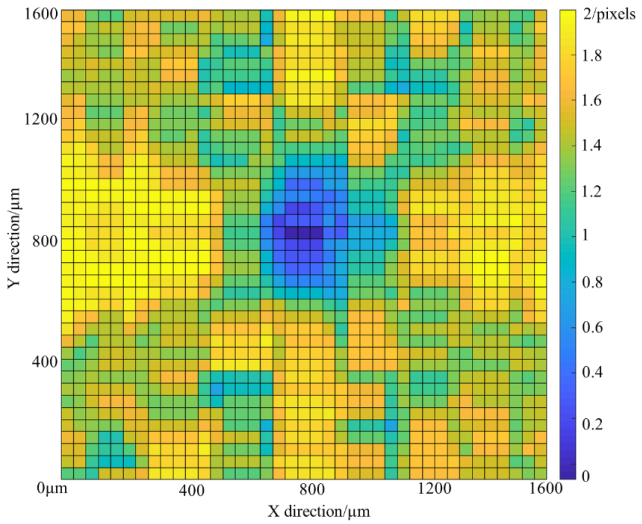

Fig. 9 Error distribution of circle detection positioning on the polar microstructure surface.

4.2 Length uncertainty and trueness

Next, the length uncertainty and trueness test were conducted. In the position measurement area,

referring to ISO 5725-1 [36], the trueness is the closeness of the mean of an arrangement of the estimated results to the genuine value and uncertainty (precision) is the closeness of assertion among an arrangement of the results. The relationship between precision and trueness is shown in Fig. 10.

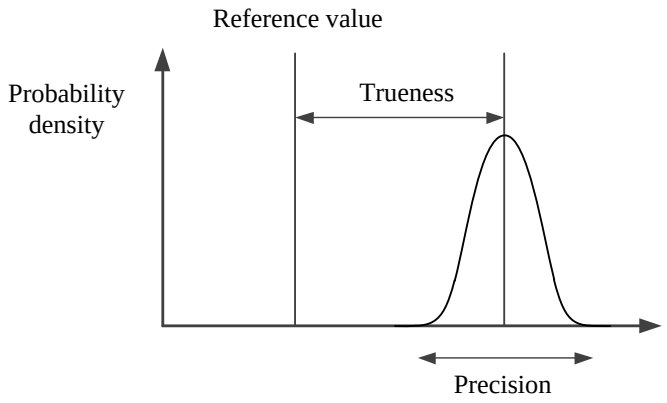

Fig. 10. Definition of precision and trueness.

An experimental setup was built to test the proposed method and obtain its uncertainty for two-axis length measurement. In this experiment, a nanometre-level piezoelectric drive stage based on a multi-sensor coordinate measuring machine (CMM) (Video-Check UA 400 3D CNC, Werth Inc., Germany) was used to test the uniaxial uncertainty and trueness of the proposed method. The CMM possesses 1 nm level resolution and 0.15 μm uncertainty of length measurement. A photograph of the experimental setup is shown in Fig. 11 (a), with the polar microstructure and its fixture mounted on the internal translator displacement drive stage of CMM. The optical system of the CMM used in this experiment consisted of a microscope and a CCD camera. The microscope was used to observe the surface of the polar microstructure, while the image was captured by the CCD camera. This piezoelectric drive stage of CMM had a resolution of 1 nm and the CCD camera had a resolution of 1021 × 1356 pixels. The camera was used together with the microscope with a magnification of 100× and a numerical aperture of 1.30. The

pixel size of the captured image was 454.200 nm in the X-axis and 453.755 nm in the Y-axis. Considering the high magnification of the microscope, Koehler illumination was chosen as the source of illumination, which gathered light to the rear of the objective lens. To test the position performance of the proposed method, an experiment was conducted to drive a 10 μm distance reciprocating 10 times each along the X- and Y-axes, and images were captured during each reciprocating cycle. Fig. 11(b) shows the sample of the captured surface image of polar microstructure. The High-precision Werth image processing (IP) video sensor for the magnification of the vision system. Subsequently, the proposed measurement method was used to determine the position of each image captured by the camera at each step.

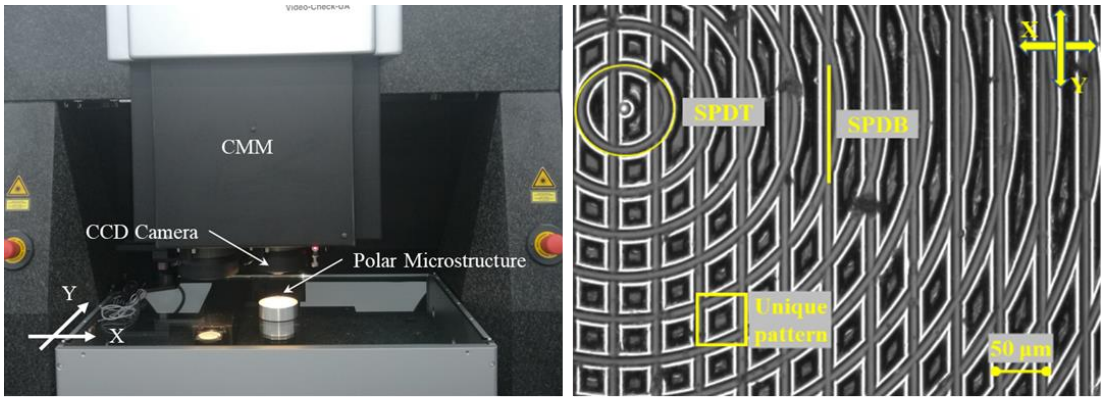

(a) (b)

Fig. 11 (a) Photograph of the experimental setup. (b) Observed surface image of the experiment

The experimental results in Figs. 12 and 13 show that the step motions were clearly distinguishable. After obtaining the data from 200 measurement points, the experimental results show that the average value of length trueness on the X-axis was –3.3 nm, and its standard deviation (uncertainty) was 92.3 nm. On the Y-axis, the average value of length trueness was 13.2 nm, and its standard deviation (uncertainty) was 93.9 nm. The results indicate that the proposed measurement method was able to

achieve 90 nm length uncertainty. In practice, owing to manufacturing and assembly errors of the workpiece, the camera may not be mounted exactly perpendicular to the surface of workpiece. In addition, the X- and Y-axis may not be perfectly orthogonal to each other. These are possible sources of error that may affect the accuracy of the measurement, and explain why the difference in trueness was different in the X- and Y-axes.

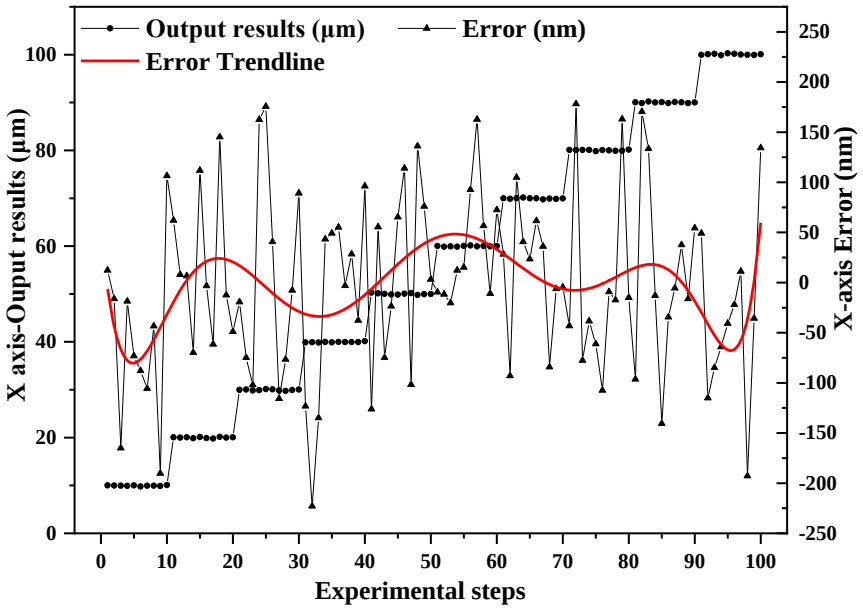

Fig. 12 Length uncertainty in the X-axis.

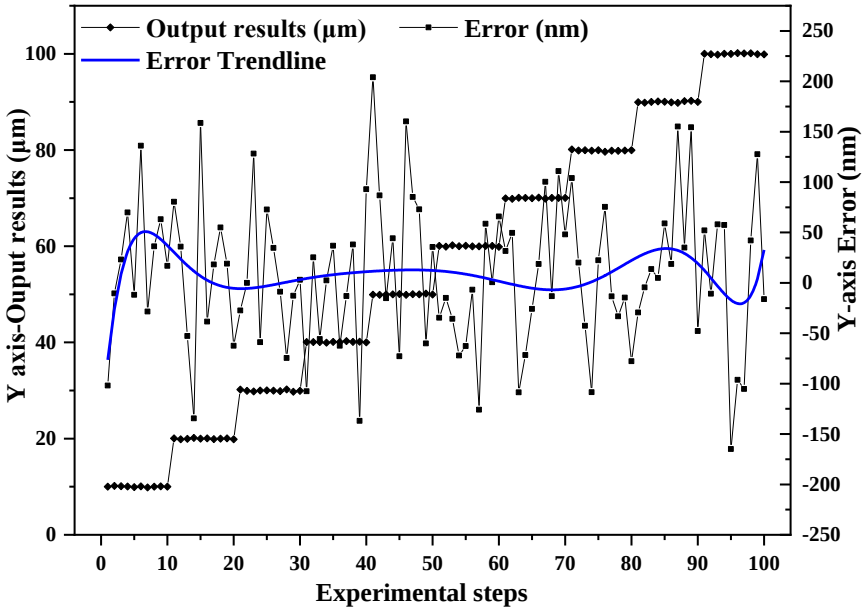

Fig. 13 Length uncertainty in the Y-axis.

4.3 Measurement speed and range

According to Eqs. (24)–(28), the calculation procedure should be repeated $(M-m+1)\times(N-n+1)$ times for the simple TM based method. For example, M and N were set to be 2000 and m and n were set to be 501, which resulted in 2.25×10^6. For the CHT-based method proposed in this paper, the number of repeated calculations would be reduced to 4×4=16 times according to the theory in Section 3.2 and the experimental results in Section 4.1. Therefore, the proposed method was 1.4×10^5 times faster than the simple TM method based on the computation time. However, the CHT and NC algorithms also incurred measurement time. To illustrate the actual measurement speed of the proposed method, a comparison of the proposed method and the original method (with only the TM algorithm) was performed. The sampling point range was 200 μm (with 20 μm spacing), and the number of sampling points was 400. Then, the positioning results of those 400 images were calculated using the proposed method and the TM method. Each calculation time was recorded automatically by Matlab®

software. A comparison of the calculation speeds is shown in Fig. 14. Although the calculation time of both the methods tended to fluctuate randomly with the measurement steps and the overall trend remained horizontal, there were obvious differences in the calculation time. The Y-axis is in the logarithmic mode to illustrate the gap between the calculation times of the proposed and the original methods clearly. The average measurement time for the original method was 2034.2 s with a standard deviation of 231.5 s, compared to 9.22 and 3.89 s for the proposed method, respectively. The results show that the proposed method had obvious advantages with regard to the calculation efficiency.

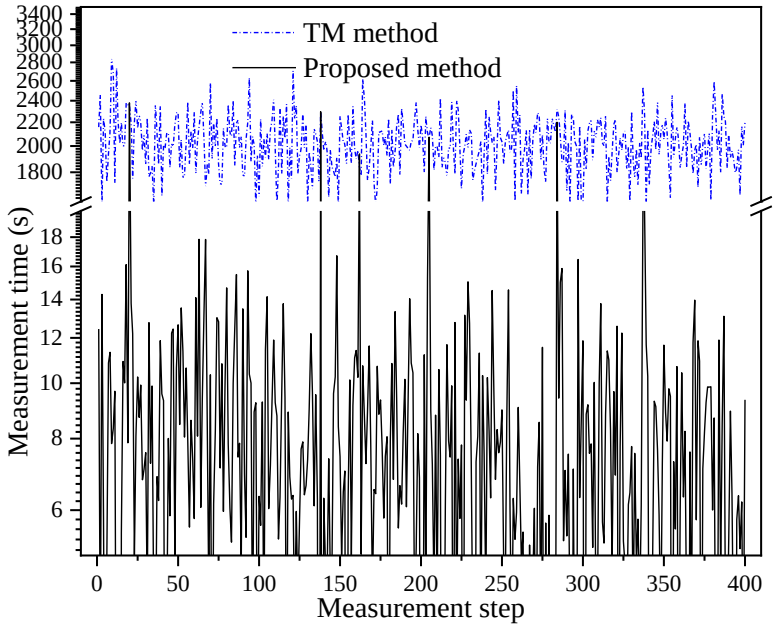

Fig. 14. Influence of the proposed method on measurement speed.

The experimental setup shown in Fig. 11 was also used to test the effective measurement range of the polar microstructure. The test length range in the X- and Y-axes was from –6.5 to +6.5 mm, with a 0.1 mm measurement spacing. The experiment involved repeating the sampling 10 times for each measurement position and then calculating its uncertainty at each position. The measurement uncertainty

results for the X- and Y-axes are shown in Figs. 15 and 16, respectively. For the X-axis, its measurement uncertainty remained stable at approximately 100 nm from –4 to +3.5 mm. However, it increased rapidly when the measurement position was away from the centre of the polar microstructure. A similar behaviour was also noticed in the Y-axis. The results in Figs. 15 and 16 show that the current allowed range of displacement was 7.5 mm in the X-axis and 7.3 mm in the Y-axis.

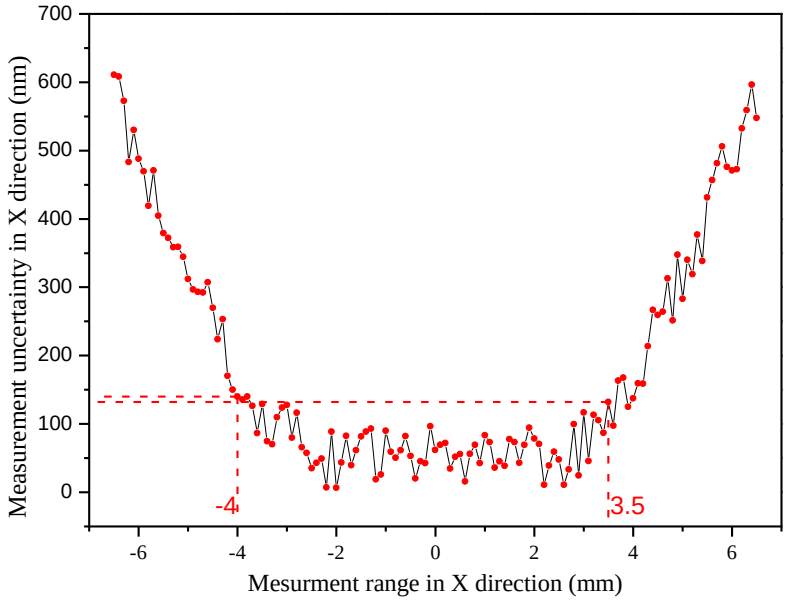

Fig. 15. Measurement uncertainty in the X-axis.

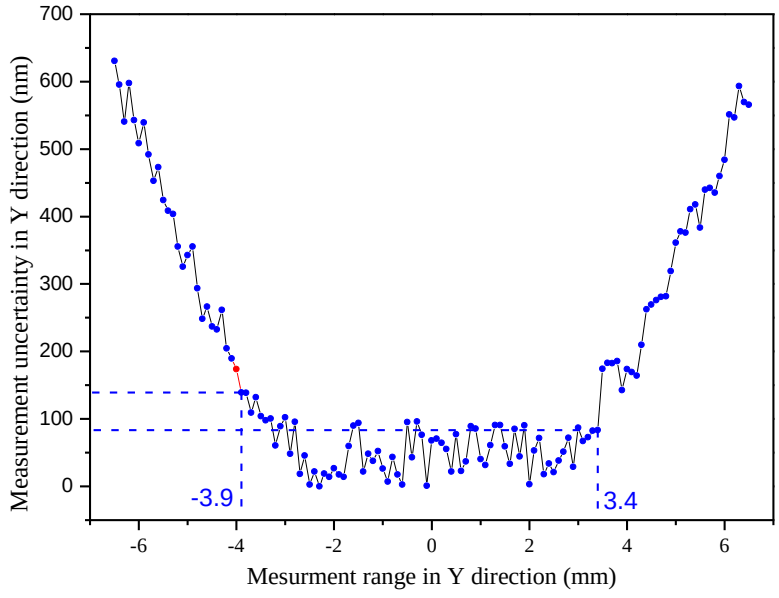

Fig. 16. Measurement uncertainty in the Y-axis.

5 Conclusion

This study presented a pattern recognition-based algorithm combined with the surface features of polar microstructure, to improve the calculation efficiency of precision positioning measurements. A specific micro-structured surface was proposed for the image processing, and a measurement system was built that included modules of CHT, NC, TM, and SI algorithms. The CHT algorithm was applied first in the precision positioning measurement, and the NC method was trained to improve the reliability of the measurement system. The SI algorithm helped to improve the measurement resolution to achieve 10 nm level. A series of validation experiments were conducted to confirm the performance of the measurement system with regard to its detection accuracy, length uncertainty, and measurement speed and range. An accuracy of over 96% was achieved in the experiment for correct circle classification, and the experimental results showed that the proposed method was able to achieve 100 nm length uncertainty. In addition, the current allowed range of displacement was 7.5 mm in the X-axis and 7.3 mm in the Y-axis. These results indicate that the proposed method is particularly suitable for fast positioning measurement.

References

[1] Gao W, Kim S W, Bosse H, et al. Measurement technologies for precision positioning. CIRP Ann 2015; 64(2): 773-96.

[2] Z. Wang, S. Gong, D. Li, D. Zhou and H. Lu H; “LED chip accurate positioning control based on visual servo using dual rate adaptive fading Kalman filter”. ISA transactions, 2019 ; Vol. 87. pp.163-173.

[3] Matić T, Aleksi I, Hocenski Ž, et al. Real-time biscuit tile image segmentation method based on edge detection. ISA Trans 2018; 76: 246-54.

[4] Shirmohammadi S, Ferrero A. Camera as the instrument: the rising trend of vision based measurement. IEEE Instrum Meas Mag 2014; 17(3): 41-7.

[5] Koch C, Georgieva K, Kasireddy V, et al. A review on computer vision based defect detection and condition assessment of concrete and asphalt civil infrastructure. Adv Eng Inf 2015; 29(2): 196-210.

[6] Chen Y H. Computer vision for general purpose visual inspection: a fuzzy logic approach. Opt Lasers Eng 1995; 22(3): 181-92.

[7] Mortara A, Heim P, Masa P, et al. An opto-electronic 18 b/revolution absolute angle and torque sensor for automotive steering applications. In: IEEE International Solid-State Circuits Conference; 2000, p. 182-3.

[8] Ruedi P F, Heim P, Gyger S, et al. An SoC combining a 132dB QVGA pixel array and a 32b DSP/MCU processor for vision applications. In: IEEE International Solid-State Circuits Conference; 2009, p. 46-7.

[9] Lee J J, Shinozuka M. A vision-based system for remote sensing of bridge displacement. NDT E Int 2006; 39(5): 425-31.

[10] Anchini R, Di Leo G, Liguori C, et al. Metrological characterization of a vision-based measurement system for the online inspection of automotive rubber profile. IEEE Trans Instrum Meas 2008; 58(1): 4-13.

[11] Minh L D, Ha C. Modeling and control of quadrotor MAV using vision-based measurement. In: IEEE International Forum on Strategic Technology; 2010, p. 70-5.

[12] Sładek J, Ostrowska K, Kohut P, et al. Development of a vision based deflection measurement system and its accuracy assessment. Measurement 2013; 46(3): 1237-49.

[13] Li Y, Li Y F, Wang Q L, et al. Measurement and defect detection of the weld bead based on online vision inspection. IEEE Trans Instrum Meas 2009; 59(7): 1841-49.

[14] Clark L, Shirinzadeh B, Bhagat U, et al. A vision-based measurement algorithm for micro/nano manipulation. IEEE/ASME International Conference on Advanced Intelligent Mechatronics 2013: 100-105.

[15] Guelpa V, Sandoz P, Vergara M A, et al. 2D visual micro-position measurement based on intertwined twin-scale patterns. Sens Actuators A Phys 2016; 248: 272-280.

[16] Guelpa V, Sandoz P, Clévy C, et al. Pattern-based vision for microrobotic manipulators calibration and servoing. In: IEEE 13th International Conference on Ubiquitous Robots and Ambient Intelligence (URAI); 2016, p. 308-10.

[17] Guelpa V, Laurent G J, Sandoz P, et al. Vision-based microforce measurement with a large range-to-resolution ratio using a twin-scale pattern. IEEE/ASME Trans Mechatronics 2015; 20(6): 3148-56.

[18] Chen Z H, Huang P S. A vision-based method for planar position measurement. Meas Sci Technol 2016, 27(12): 125018.

[19] Korolev A N, Lukin A Y, Polishchuk G S. Use of information redundancy in optical digital measurement systems with 2D sensor. Meas Tech 2017; 60(3): 242-47.

[20] Kim J A, Kim J W, Kang C S, et al. Note: An absolute XY-Θ position sensor using a two-dimensional phase-encoded binary scale. Rev Sci Instrum 2018; 89(4): 046105.

[21] Galeano-Zea J A, Sandoz P, Gaiffe E, et al. Pseudo-periodic encryption of extended 2-D surfaces

for high accurate recovery of any random zone by vision. Int J Optomechatroni 2010; 4(1): 65-82.

[22] Galeano J A Z, Sandoz P, Gaiffe E, et al. Position-referenced microscopy for live cell culture monitoring. Biomedl Opt Express 2011; 2(5): 1307-18.

[23] Li H, Zhang X, Zhu B. Single grid image based calibration of an optical microscope. In: IEEE International Conference on Manipulation, Automation and Robotics at Small Scales (MARSS); 2017, p. 1-6.

[24] Zhao C, Cheung C F, Liu M. Nanoscale measurement with pattern recognition of an ultra-precision diamond machined polar microstructure. Precis Eng 2019; 56: 156-63.

[25] Zhao C, Cheung C, Liu M. Integrated polar microstructure and template-matching method for optical position measurement. Opt Express 2018; 26(4): 4330-45.

[26] Zhao C, Cheung C, Liu M. Modeling and simulation of a machining process chain for the precision manufacture of polar microstructure. Micromachines 2017; 8(12): 345.

[27] Zhao C, Cheung C F. Theoretical and experimental investigation of the effect of the machining process chain on surface generation in ultra-precision fly cutting. Int J Adv Manuf Technol 2018; 99(9-12): 2819-31.

[28] Xia H, Zhao W, Jiang F, et al. Fast template matching based on deformable best-buddies similarity measure. Multimed Tool Appl 2019, 78(9): 11905-25.

[29] Toyama F, Mori H, Shoji K. Fast template matching using Brick Partitioning and initial threshold. In: IEEE 23rd International Conference on Pattern Recognition (ICPR); 2016, p. 687-1.

[30] Jenkins M D, Barrie P, Buggy T, et al. Extended fast compressive tracking with weighted multi-frame template matching for fast motion tracking. Pattern Recogn Lett 2016; 69: 82-87.

[31] Zhang S J, To S, Wang S J, et al. A review of surface roughness generation in ultra-precision

machining. Int J Mach Tool Manuf 2015; 91: 76-95.

[32] Mukhopadhyay P, Chaudhuri B B. A survey of Hough Transform. Pattern Recognit 2015; 48(3): 993-1010.

[33] D'Orazio T, Guaragnella C, Leo M, et al. A new algorithm for ball recognition using circle Hough transform and neural classifier. Pattern Recognit 2004; 37(3): 393-408.

[34] Cilimkovic M. Neural networks and back propagation algorithm. Institute of Technology Blanchardstown, Blanchardstown Road North Dublin, 2015, 15.

[35] Schmidhuber J. Deep learning in neural networks: An overview. Neural network 2015; 61: 85-117.

[36] ISO. Accuracy (trueness and precision) of measurement methods and results-Part 1: General principles and definitions. International Organization for Standardization, Geneva, 1994.